High-Temperature Operation of v-MoS₂ Nanowalls/TiO₂ Photodetectors with Excellent Performances

Xiaoyan Peng^{1,2}, Jiazheng Chen¹, Shun Wang¹, Lidan Wang¹, Shukai Duan¹, Peter Feng², Jin Chu¹

¹ Chongqing Key Laboratory of Brain-Inspired Computing and Intelligent Control, College of Artificial Intelligence, Southwest University, Chongqing 400715, China

²Department of Physics, University of Puerto Rico, San Juan, PR 00931, USA

Corresponding author: Jin Chu (chujin@swu.edu.cn).

Abstract:

It is a challenging task to fabricate thermally stable Photodetectors (PDs) working in visible light spectrum range due to the degradation in photoresponse characteristics. Herein, excellent performance parameters with photoresponsivity reached up to as high as 50 AW-1, and ultrahigh specific detectivity in excess of 2.3×10^{12} Jones have been obtained simultaneously in a single photodetector based on vertical MoS₂ (v-MoS₂) at a high temperature of 200°C. The TiO₂ interlay layer is ascribed as the main factor to enhance the PDs performances by reducing lattice mismatch between v-MoS₂ and substrate, separating photogenerated electron-hole pairs (EHPs), and the formation of the vertical MoS₂ nanostructures. Besides, the optoelectronics performances of the v-MoS₂/TiO₂ heterostructures based field-effect transistor (FET) have also been examined under various operating temperatures, and the mechanism on how gate voltages affect the PDs performances has also been studied. In a word, the present fabricated v-MoS₂/TiO₂ heterostructures based FET PDs will find practical applications in high-temperature environment.

1. Introduction

As a typical device that efficiently converts optical signals to electrical signals, photodetectors (PDs) have been widely used in the fields of medical instruments, pollution analyzers, flame monitoring, and astronomy [1]. Recently, MoS₂ has been highly interested in being developed as PDs owing to the high density of surface states, excellent optical

absorption characteristics [2], and satisfactory carrier mobility [3]. The above unique characteristics facilitate 2D MoS₂ achieving high photosensitivity and the increased lifetime of a photocarrier. Another important aspect that makes MoS₂ a good candidate for PDs is its tunable bandgap width, which is very helpful in designing multispectral PDs. Compared to the parallel MoS₂ nanosheets (p-MoS₂), MoS₂ nanosheets with vertical arrangement (v-MoS₂) have raised great interest for their large surface to volume ratio, catalytically active sites [4], and a large number of exposed edges with extensive dangling bonds [5]. These properties make it highly promising in the field of PDs. However, there is a tough puzzle in the fabrication of high performances PDs devices with MoS₂. The PDs based on single nanomaterials show low optoelectronic performance, such as unsatisfactory responsivity or narrowband usage, due to the limitation of collecting photogenerated electron-hole pairs (EHPs). Thus, the PDs based on hybrid or composite nanomaterials are usually synthesized to modulate the photoresponse characteristics to a large extent [6].

Normally, the temperature of PDs is always raised by absorbing light energy because the absorption area of PDs is always close to the irradiated source in order to obtain a high absorption coefficient of various spectral lights [7]. Hence, high thermal stability is required for PDs' material. Meanwhile, for flame detection and explosive environmental applications, the PDs capable of operating at high temperature are of great importance [8]. Several materials like AlGaN [9], GaN [10], Ga₂O₃ [11], and CuO₃ [12] had been utilized immensely to design and develop as PDs. However, the high-performance PDs made of those nanomaterials worked at high temperatures are still difficult to obtain.

The traditional silicon-based PDs are sensitive to temperature fluctuation, and dark currents will be significantly elevated at high temperatures [13], leading to limited practical applications. Hence, it is still a challenge to fabricate the PDs with enhanced high-temperature performances via effective processes. Furthermore, the low performances of PDs at high temperature are normally attributed to the large dark current generated from the lattice mismatches between detecting materials and substrates [14], or transitions of EHPs between narrow bandgap. Therefore, the realization of PDs with good-performance based on the relatively low bandgap of MoS₂ (~1.8 eV for multiply layer) in contrast to

other materials for PDs e.g., GaN of 3.36 eV, ZnSTe of 3.6 eV, SiC of 2.2 eV, and SiCNs of 3.77 eV, is even more difficult in a high temperature environment.

Here, we have successfully fabricated high-performance PDs based on chemical vapor deposition (CVD) v-MoS₂ nanowalls on Si substrate using TiO₂ as an induction layer. The usage of the TiO₂ buffer layer induced the growth direction of MoS₂ changing from parallel to vertical. The aggregation of TiO₂ caused the increase in surface roughness, which helps to the nucleation of MoS₂ during CVD growth process [15]. The photoresponsivity, detectivity, photocurrent and response time of the PD devices were influenced by many factors as bias voltage, light illumination density, operating temperate, and gate voltage, etc. The PDs presented here have remarkably large photoresponsivity and detectivity at various experimental conditions, making it possible to apply in harsh environment detection.

2. Experimental

The TiO₂ induction layer and MoS₂ nanostructures were grown on n-type Si substrates by a chemical vapor deposition (CVD) system. Prior to the MoS₂ growth, the Si substrates with a 300 nm thick SiO₂ insulating layer were pretreated as follows: The substrates were successively put into ultra-pure water, ethanol, and acetone for 20 min by ultrasonic. And then, the substrates were stored in alcohol for keeping clean. TiO₂ thin film with a 20 nm thickness was deposited on the prepared substrate as induction layer by magnetron sputtering method for 30 s.

Then, the Argon gas was introduced with a flow of 70 sccm into the quartz tube of CVD furnace. The optimization of both the ratio of precursors and the gas flow is important for the v-MoS₂ nanowalls formation. The sulfur powder (0.5 g) was placed at the entrance of the CVD furnace, and the substrates were buckled upside down on a quartz boat containing molybdenum trioxide (MoO₃) powders (0.02 g) in the center of the furnace. The temperature inside the tube was kept at 800 °C for 30 min. Then, the samples were cooled down to room temperature (RT) naturally. For comparison, a pure MoS₂ nanostructure sample was also synthesized under the coincident experimental conditions except for the absence of TiO₂ layer.

The nanostructures and morphologies of the as prepared samples were characterized by scanning electron microscopy (SEM) and transmission electron microscopy (TEM) (VEGA3SBH, Tescan and JEM2100). The chemical compositions and bonds were determined by energy dispersive X-ray spectroscopy (EDS) and X-ray photoelectron spectroscopy (XPS). Raman measurements were performed using a microsystem with a laser wavelength of 514 nm (LabRAM HR Evolution, Horiba), and the crystal structures were determined by x-ray diffraction (XRD) with Cu/Ka radiation.

After surface characterizations, Ti (30 nm) and Au (60 nm) double-layered metal electrodes were deposited by e-beam evaporation technique on both sides of the sample for optoelectronic characterizations. The probe station (JANIS ST-500) with various lights and a semiconductor device analyzer (Agilent B1500A) were used to measure the electrical and optoelectronic characteristics properties. To further explore the PDs' performance, the response behaviors to light sources were also tested under different bias voltages, light power densities, gate voltages, and temperatures.

3. Result and discussion

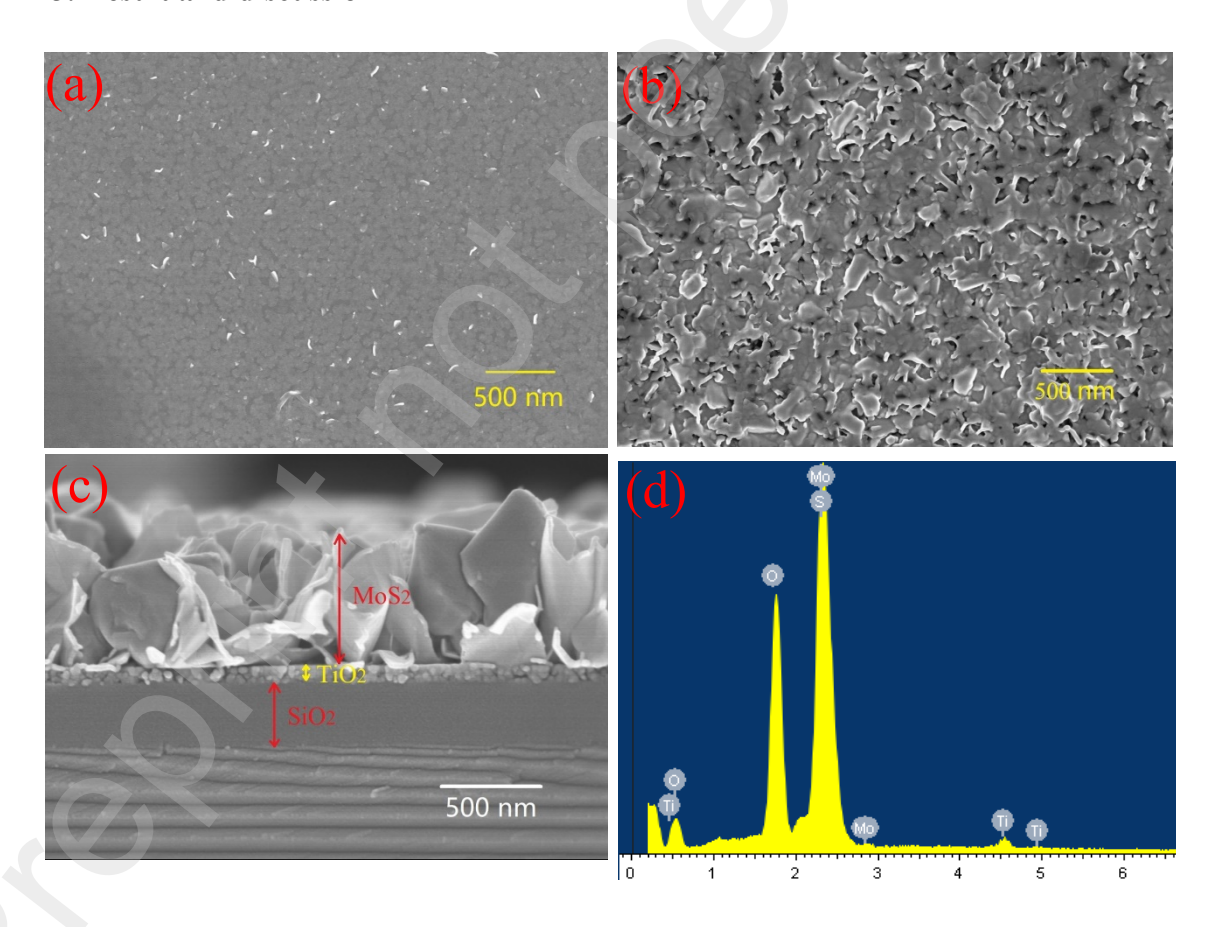


Fig. 1 Top-view SEM images of (a) p-MoS₂ thin film, (b) v-MoS₂/TiO₂ heterostructures; (c) cross-section SEM images, and (d) corresponding EDS spectrum of v-MoS₂/TiO₂ heterostructures.

Top-view SEM images show the P-MoS₂ thin film and v-MoS₂ nanowalls with sharp edges are uniformly distributed on the surface of the substrate, as exhibited in Fig. 1(a) and (b), respectively. Fig. 1 (c) shows the cross-section image of v-MoS₂/TiO₂ heterostructures, proving the existence of 20 nm TiO₂ interlayer and the v-MoS₂ nanowalls with a height of approximately 200 nm. The formation of the v-MoS₂ nanowalls was ascribed to the p-MoS₂ thin film extrusion and upward growth. The extrusion was origin from the gradient strain effect caused by the thermal agglomeration of the TiO₂ film during the growth process [16-17]. The EDS spectrum (Fig. 1 (d)) indicates the existence of Mo, S, Ti and O elements with atomic ratios of S/Mo and O/Ti approximately 2:1 and 2.6:1, respectively.

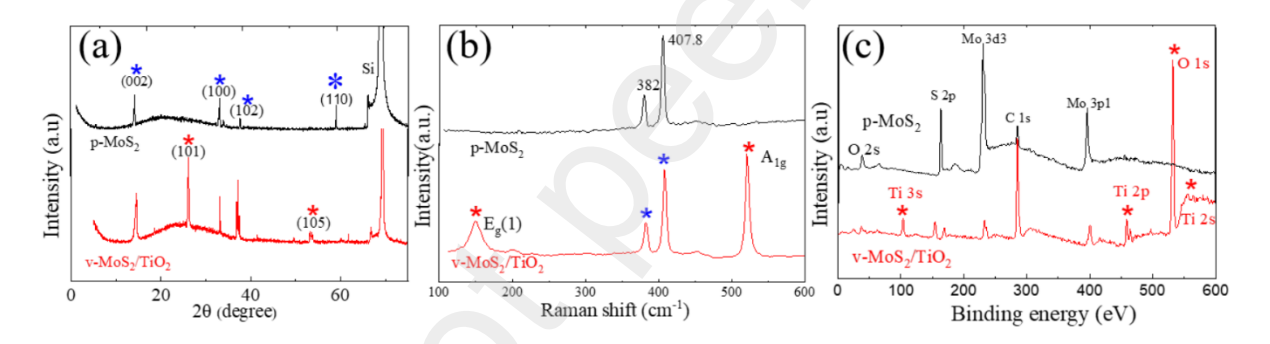


Fig. 2 Comparison of (a) XRD patterns, (b) Raman, and (c) XPS survey spectra of p-MoS₂ thin film and v-MoS₂/TiO₂ heterostructures.

Nanocrystalline structure and compositions analysis of p-MoS₂ and v-MoS₂/TiO₂ heterostructures were conducted by XRD, Raman and XPS, respectively. The diffraction peaks of TiO₂ (marked with red stars) in the XRD pattern (Fig. 2(a)) are well indexed to anatase TiO₂ [18], with two peaks appearing at 25.1° and 52.6° are assigned to (101) and (105) orientations, respectively. As for the MoS₂, the diffraction peaks (marked with blue stars) found at 14.1°, 32.9°, 39.5° and 58.7° correspond to (002), (100), (102), and (110) hexagonal crystallographic planes.

The Raman spectra shown in Fig. 2 (b) clearly illustrate the crystalline structures of the two samples. The peaks at 382 and 407.8 cm⁻¹ could be ascribed as the in-plane E_{2g}^1 and

out-of-plane A_{1g} modes of hexagonal MoS₂. The difference between E_{2g}^1 and A_{1g} is 25.8 cm⁻¹, indicating multilayer of MoS₂. The peaks belonging to TiO₂ at 149 cm⁻¹ is the E_g (1) mode arising from symmetric stretching of O atoms around the Ti atom [19]. Another peak A_{1g} of anatase TiO₂ located at 520.6 cm⁻¹ is red shifted with respect to the pristine TiO₂. In this case, the redshift is an indication of small scaled agglomeration of nanocrystalline TiO₂ caused by the uncertainty principle [20]. The agglomeration is a benefit to the formation of vertical growth of MoS₂ nanowalls, as illustrated previously.

XPS analysis was utilized to check the surface chemical bonding properties and the surface composition of two samples. As displayed in Fig. 2 (c), the full-scan XPS spectrum survey indicates that the main elements are Mo, S, Ti, O, and C for the v-MoS $_2$ /TiO $_2$ heterostructures, which reveals the successful heterojunction loading of MoS $_2$ and TiO $_2$. The elements Mo, S, Ti, and O elements were from the prepared v-MoS $_2$ /TiO $_2$ heterostructures, and the C element was from the XPS instrument itself. Also, the XPS data of v-MoS $_2$ /TiO $_2$ heterostructures show the element concentration are well fitted to the EDS data.

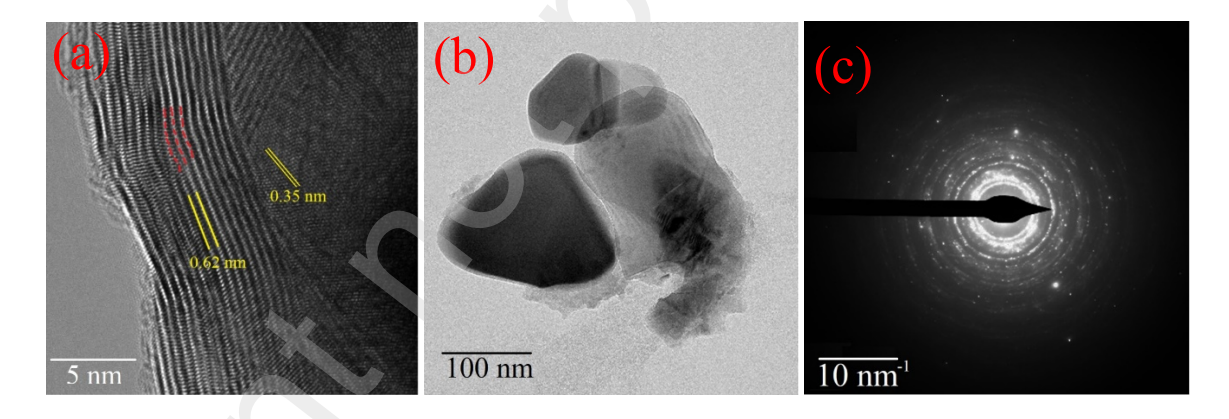


Fig. 3 (a) HRTEM, (b) TEM, and (c) selected area electron diffraction (SEAD) spectrum of the v-MoS₂/TiO₂ heterostructures.

Fig. 3 (a) shows the lattice spacing of 0.35 nm and 0.62 nm, corresponding to (101) lattice plane of anatase TiO₂ and (002) lattice plane of hexagonal MoS₂. Fig. 3(b) presents the overlapping multi-layer morphology of MoS₂ agglomerated with adjacent nanosheets. The SAED pattern of the sample is also measured, as seen in Fig. 3(c). The exhibited diffraction rings were mostly caused by well pronounced spots indexed to MoS₂ and

anatase TiO_2 , demonstrating polycrystalline of the v-MoS₂/TiO₂ nanocomposite phases. The above measurements are applied to examine the interface status of v-MoS₂/TiO₂ and prove that the superimposed diffraction patterns of TiO_2 and MoS_2 can be distinguished.

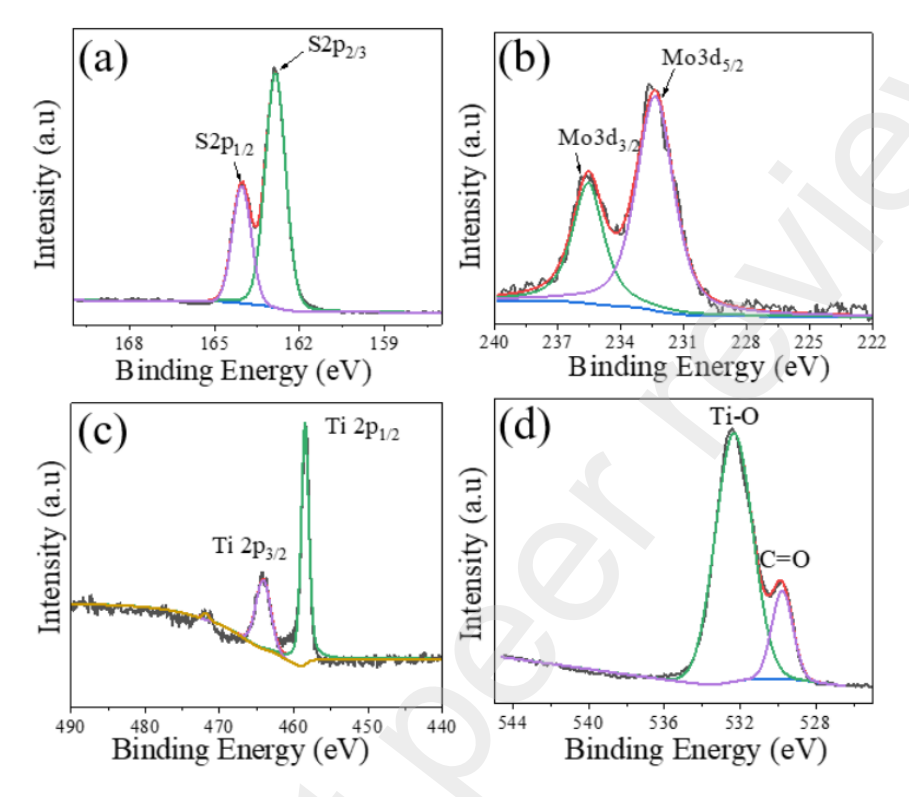


Fig. 4 The deconvoluted high-resolution XPS spectra of (a) S 2p, (b) Mo 3d (c) Ti 2p, (d) O 1s of v-MoS₂/TiO₂ heterostructures.

The deconvoluted high-resolution XPS spectra of v-MoS₂/TiO₂ heterostructures show the binding energy of S 2p, Mo 3d, Ti 2p, and O 1s peaks located at 162, 233, 459, and 529 eV in the XPS survey spectrum, respectively. Fig. 4(a) shows the binding energy of S2p state in the v-MoS₂/TiO₂ sample. The binding energies of S 2p 3/2 and S 2p ½ are 163.1 eV and 164.5 eV, respectively, indicating the S²⁻ form in the composite. Furthermore, the peaks at 164.5 eV is assigned to the existence of Mo-O-S or S on the surface of MoS₂ [21]. The spectrum of Mo 3d in Fig. 3(b) demonstrates two peaks located at 232.13 eV and 235.6 eV, assigned to Mo 3d 5/2 and Mo 3d 3/2, respectively, indicating the existence of Mo⁴⁺ [22]. Fig. 4(c) displays that the binding energy of Ti 2p 3/2 and Ti 2p 1/2 are 458.3 and 464.1eV respectively, which belongs to the Ti⁴⁺ [23]. In Fig. 4(d), the main peaks observed at at 529.8 eV and 532.3 eV can be ascribed to lattice oxygen, Ti-O and C=O [24]. The hydroxyl may come from air ambient during the sample transfer process.

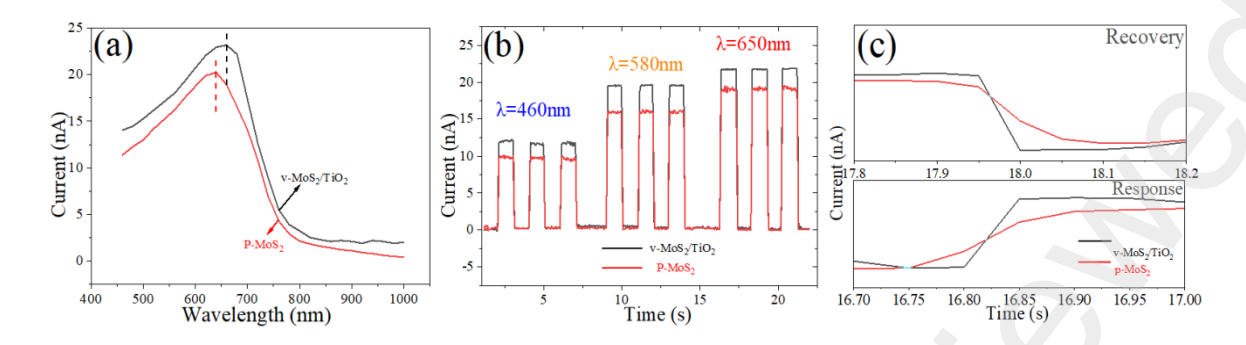


Fig. 5 (a) A spectroscopic photoresponse under a broad band ranging from 450 nm to 1000 nm; (b) The current responses at three different illumination wavelengths, and (c) The response and recovery time to 650 nm light of the two PDs. All the experiments were conducted at RT without bias. The light power density is 1.6×10^{-6} W/cm².

The optoelectronic characteristics of the two PDs are studied after surface characterizations. Lights with various wavelengths were illuminated on the detecting materials connected by one pair of Ti/Au electrodes, and the photoresponse was measured by a two-probe method. Fig. 5(a) represents a spectral response of two PDs, indicating both devices are insensitive to the illumination with a light wavelength longer than 750 nm. When the wavelength is shorter than 750 nm, the responsivity increases gradually and reaches maximum values at about 650 nm and 640 nm for two PDs, respectively. The peak location of the pure MoS₂ based PD demonstrates that the photocurrent is mainly from the photoexcited EHPs with the energy higher than the bandgap of hexagonal MoS₂ material. The redshift of the peak to 650 nm for the v-MoS₂/TiO₂ based PD indicates the decrease of the bandgap of the material attributed to the existence of the TiO₂ induction layer.

But further wavelength shortening after 650/640 nm causes a drop in current. Since the recombination rate of photogenerated EHPs near the surface region exceeds that in MoS₂ bulk materials. Thus, increasing absorption of high energy photons at a short wavelength (less than 650/640 nm) range will accelerate the recombination and consequently lower the photocurrent across the PDs [25]. The peak position differential of two photoresponse vs wavelengths in Fig. 5(a) may be due to bound-to-continuum electron transitions and bound-to-bound transitions originating from the corresponding energy spacing of the v-MoS₂/TiO₂ and MoS₂ nanowalls.

The effect of illumination wavelengths on the current transient behavior is clearly displayed in Fig. 5(b). The time-dependent photoresponses of the two PDs were measured

by periodically switching in the repetitive cycling test for all three lights, showing good stability and high reversibility for two PDs. Two PDs are very efficient in producing EHPs when exposed to 650 nm light since the wavelength is the closest to the bandgap of MoS₂ nanomaterials and thus produces the highest photocurrent values [26]. The photocurrents of two PDs to three wavelengths lights are around 10 to 20 nA, as exhibited in Fig. 5 (b).

The response and recovery times of the two PDs under 650 nm light illumination are presented in Fig. 5 (c). The fall and rise in current in response to light illumination on the PD can be expressed by the expression:

$$I(t) = I_0 + A_{1e}^{-(t-t_0)/\tau_1} + A_{2e}^{-(t-t_0)/\tau_2}$$
(1)

where I_0 is the dark current in this case; t is the time, scaling factors are denoted by A_1 and A_2 ; the time constants are τ_1 and τ_2 ; It is displayed that the photoresponse/recovery time is faster than 0.1 s from the magnified view of a ON/OFF cycle in Fig. 5 (c). Fast photoresponse/recovery speeds were achieved due to quick separating and recombining EHPs because of the high density of surface state and narrow energy bandgap of the two PDs. The reduced recovery time of the v-MoS₂/TiO₂ based PD is owing to the larger surface/volume ratio of the v-MoS₂ nanowalls than that of the p-MoS₂. Since a larger amount of dangling bond on the v-MoS₂ surface can serve as recombination centers and consequently, it would accelerate the recombination of EHPs [27].

Compared with the PD based on pure MoS₂, the v-MoS₂/TiO₂ PD shows higher sensitivity and faster photoresponse/recovery. Since two processes originated from surface states and EHPs are contributed to photoresponse behaviors, the significantly improved performances of the v-MoS₂/TiO₂ heterostructures can be ascribed to: (1) The high surface states density and high specific surface-area v-MoS₂, in which electrons are the dominated carrier. Holes traps on the surface of v-MoS₂ are conducive to the multiple electrons pass, resulting in photoconductive gain [28]. (2) The appropriate space among vertical nanowalls can be served as a light mirror and allows refraction and reflection of light inside the surface of the v-MoS₂. Therefore, the photocurrent is enhanced by multiple refraction and reflections of light waves. (3) The reduction of lattice mismatch between photoactive layer and substrate. The hexagonal MoS₂, anatase TiO₂, and SiO₂ are normally supposed to be with lattice constant c of ~12.53 nm, 9.51 nm, and 5.4 nm, respectively. The TiO₂ induction layer is acted as a lattice-matching transformer between the MoS₂ and the SiO₂ surface.

During the growing of the MoS_2 on the surface of the TiO_2 , parts of Ti and O atoms are gradually substituted by atom Mo or atom S. Since the atomic radius of Mo and S are larger than that of Ti and O, the lattice of the TiO_2 layer is expanded continuously to the MoS_2 . Therefore, the lattice mismatch between SiO_2 and MoS_2 can be decreased automatically.

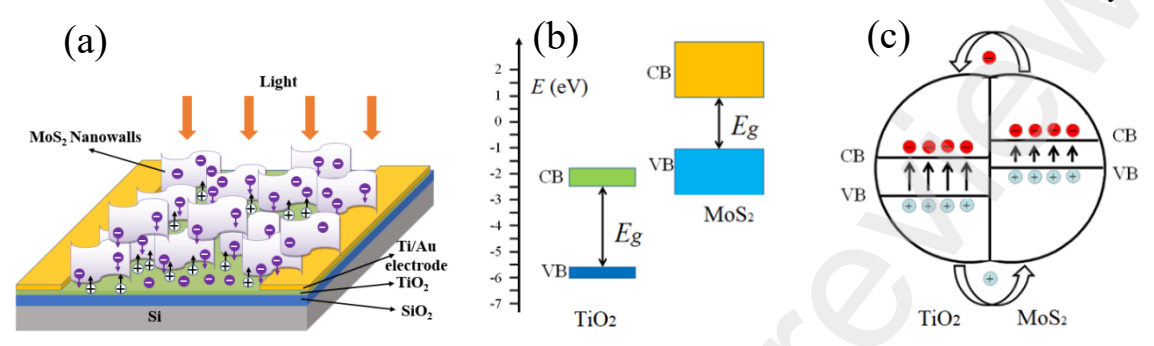


Fig. 6 Schematic diagram of (a) the fabricated device; (b) conduction band (CB) and valence band (VB) positions of TiO₂ and MoS₂; (c) generation and transfer of photogenerated EHPs at TiO₂ and MoS₂ heterogeneous interface with staggered energy band structure.

The band structures of the v-MoS₂/TiO₂ also contribute to better performance than the planar counterpart. The schematic diagram of the PD device and the CB/VB positions of TiO₂ and MoS₂ are shown in Fig. 6, exhibiting a staggered energy band structure of the heterostructures. The large specific surface area of the v-MoS₂ based PD can provide a longer photon transfer path than that of a parallel aligned structure [29]. The high detecting performances are mainly attributed to photogenerated EHPs transfer and carrier separation between the interfaces of v-MoS₂/TiO₂ heterogeneous. Since the CB position of TiO₂ is higher than the VB position of MoS₂, a large number of EHPs can be rapidly separated, and a large photocurrent is induced.

In summary, the v-MoS₂/TiO₂ nanostructures have advantage of high surface to volume ratio, high photo utilization, long photon path length [30], and carrier exchange between heterostructures. Since v-MoS₂/TiO₂ heterostructures based PD shows good photoresponse to 650 nm light, the study would emphasize on this in the following experiments.

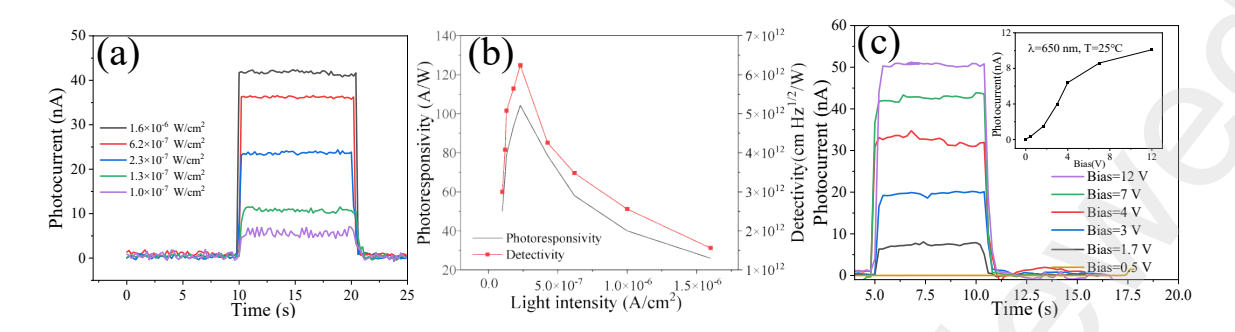


Fig. 7 (a) Photocurrent under various light power densities under 0 bias (b) photoresponsivity and detectivity as a function of light power density, and (c) photoresponse behaviors under different bias and photocurrent as a function of bias of the v-MoS₂/TiO₂ PD at 1.0×10⁻⁷ W/cm² light illumination and RT (inset).

Fig. 7 (a) shows the photocurrents of the v-MoS₂/TiO₂ under 650 nm light with various light power densities at RT without any bias, demonstrating the photocurrent is completely excited by the light illumination. Increasing light power density induces enhanced photocurrent, and the photogenerated EHPs rate is proportional to the illumination photon flux. The corresponding dependence is well fitting to the well-known power law [31]. The enhanced photocurrent can be attributed to the rise in Fermi energy and fall in work function caused by increasing carrier density [32].

Photoresponsivity (R_{λ}) and detectivity (D^*) are critical parameters of the MoS₂ PDs to evaluate the capacity of PD converting the light signals to electrical signals and detecting a weak signal under a certain wavelength, respectively. The expressions of R_{λ} and D^* are as following:

$$R_{\lambda} = \Delta I_{ph} / P_{\lambda} \tag{2}$$

$$D^* = R_{\lambda} \times \sqrt{A} / \sqrt{2qI_{dark}} \tag{3}$$

where ΔI_{ph} is the photo-excited current ($\Delta I_{ph} = I_{light} - I_{dark}$), P_{λ} is the light power density, and A is the effective area of the PD. In Equation (2), q is the absolute value of the electron charge, I_{dark} is the current density in the dark.

A comparison performance of the PD under different light power density is exhibited in Fig. 7 (b), from where the device shows a high responsivity and specific detectivity values under extremely low light power density. The highest values of R_{λ} (=130 A/W) and

 D^* (= 6 × 10¹² J) are recorded at a light power density of 1.6×10⁻⁶ W/cm². However, the light power density higher than that induced lower values of R_{λ} and D^* , indicating the photoexctied generation rate becomes lower at this condition.

Next, we fixed the illumination power density of the light to the minimum value (1.0 $\times 10^{-7}$ W/cm²). The dependency of photocurrent on bias voltage was investigated for the v-MoS₂/TiO₂ PD, as exhibited in Fig. 7 (c) and the right-hand-side inset in Fig. 7 (c). When the bias voltage applied across the metal-semiconductor-metal structure device increases, the photoexcited EHPs separated by the bias voltage increases accordingly, and thus a raised photocurrent could be generated [33].

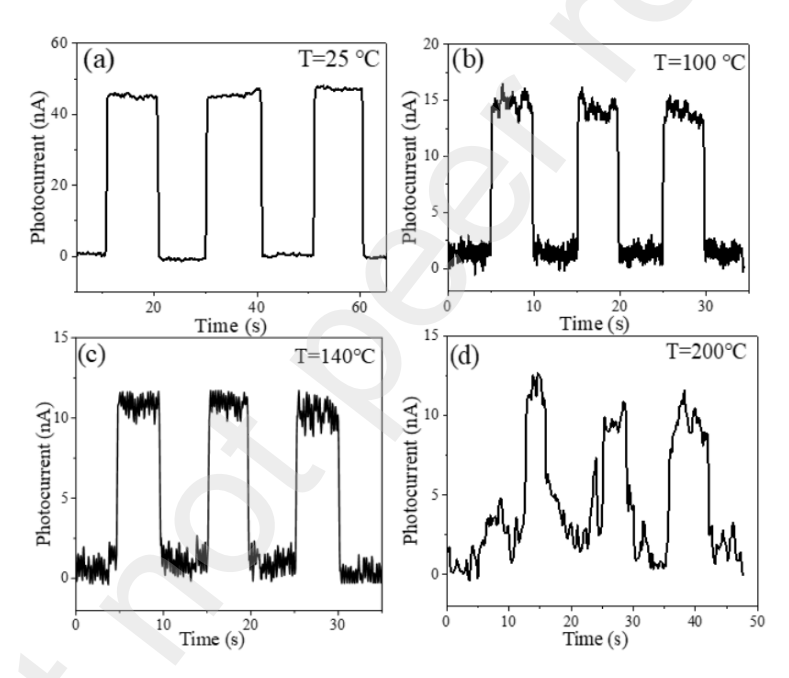


Fig. 8 Photoresponse behaviors of v-MoS₂/TiO₂ to 650 nm light under different temperature (a) 25 °C, (b) 100 °C, (c) 140 °C, (d) 200 °C. All the measurements are performed with a power density of 1.6×10⁻⁶ W/cm² and a bias of 0.5 V.

It is very important for PDs to have reliable stability when working at high temperatures. The photocurrents under different temperatures ranging from 25 to 200 °C were measured, as shown in Fig 8. The lowering of the photocurrent value and signal-to-noise ratio at a high temperature can be clearly observed, which is attributed to the consecutive growing in dark current with temperature [34]. It is observed that 650 nm light can be detected by the v-MoS₂/TiO₂ PD even at 200 °C, with high photoresponsivity and detectivity of 39

A/W and 1.8×10^{12} J, respectively. Although noise to signal ratio is increasing with temperature, the photoresponse peaks to light illumination can still be visible.

It is worth mentioning here that the high incident power density normally creates unavoidable heating effect in the layered materials [35]. However, the power density in our case was too small to induce any temperature enhancement in the device. Moreover, at a high temperature of 200 °C, the Joule heating is calculated to be as negligibly small as 10^{-8} J. Therefore, the v-MoS₂/TiO₂ PD has been found to be promising even at high temperature because light heating has no obvious influence on the performance of the device.

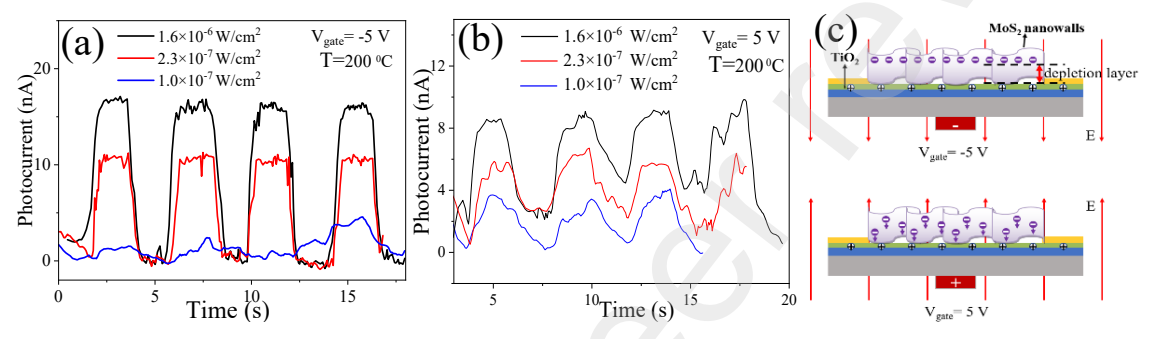


Fig. 9 Photocurrent of a v-MoS₂/TiO₂ FET to 650 nm light under various light power density at gate voltages of (a) -5V, (b) 5V, and (c) Mechanism diagram of the effect of gate voltage on detecting performance of v-MoS₂/TiO₂.

To improve the high-temperature performances of the fabricated PD, gate voltages of 5 V and -5 V across the device were applied with a bias of 0.5 V under various power density. The effect of gate voltage is clearly reflected in Fig. 9. The device shows improved performances under -5 V gate voltage (Fig. 9 (a)), with improved photoresponsivity and detectivity of 50 A/W and 2.3×10^{12} J, respectively. On the contrary, the different photoresponse behaviors were observed under 5 V gate voltage (Fig. 9 (b)).

The electrons and holes get separated to the band of MoS₂ and TiO₂, respectively, because of the presence of the upwards electric field created by the applied -5 V gate voltage. The separation of the EHPs leads to the depletion layer between the v-MoS₂/TiO₂, while the opposite situation happens (or happened) when 5 V gate voltage is (or was) applied, as illustrated in Fig. 9 (c).

Table 1. Summary of the PDs based on 2D nanosheets and related materials.

Device	R_{λ}	D^*	Response	Recovery	T	Ref.
	(A/W)	(Jones)	$time(\mu s)$	$time(\mu s)$	(K)	
Multilayer MoS ₂	50.7×10-3	1.55×109	/	/	RT	[36]
Dye-Sensitized MoS ₂	1.17	1.5×10 ⁷	5.1	2.3×10 ⁶	RT	[37]
$Encapsulated \ MoS_2(with \ Gate \ Controllable)$	~104	≥ 7.7 × 10 ¹¹	8×10 ³	/	RT	[38]
MoS ₂ (Driven by Ferroelectrics)	2570	2.2×1012	1.8×10 ³	2.0×10 ³	RT	[39]
2H-MoS ₂ /1T@2H-MoS ₂	1917	~7.55×10 ¹¹	/	1	RT	[40]
$Graphene/InSe/MoS_2$	110×10-3	>1010	~1×10 ³		RT	[41]
$Graphene/MoO_3/MoS_2$	670×10-3	4.77×10 ¹⁰	/	*	RT	[42]
Reduced graphene oxide/MoS ₂	~2.1	~5×10 ¹¹	18×10 ³	1	RT	[43]
InAs-GaAs Quantum-Dot	0.3	1011		1	175	[44]
Multi-Layered(100) Facet-Oriented β-Ga ₂ O ₃ nanobelts	~851	/	~3×10 ⁵	~3×10 ⁵	433	[31]
GaSe Nanosheet-Based	4.5	1.0×10 ¹²	0.7×10 ⁶	1.2×106	393	[45]
$v\text{-MoS}_2/\text{TiO}_2 \text{ heterostructures FET}$	130	6.4×10 ¹²	<100	<100	473	[this work]

The detecting performances enhancement of V-MoS₂ by applying -5V gate voltage in comparison without gate voltage, is comparable with previously reported values (table 1). They includes: several kinds of nanostructured MoS₂, such as: multilayer MoS₂, encapsulated MoS₂ controlled by gate voltage, and MoS₂ PD driven by derroelectrics [36-39], or MoS₂ composites or heterostructures, like 2H-MoS₂/1T@2H-MoS₂, Graphene/InSe/MoS₂, Graphene/MoO₃/MoS₂, and reduced graphene oxide/MoS₂ [40-43]. Although good detecting performances these PDs exhibited, they are all worked at RT. Also, several PDs were designed to work at high temperature [31, 44-45]. The PD based on v-MoS₂/TiO₂ with -5 V gate voltage in this work displays a satisfied performance with ultrahigh photoresponsivity and detectivity, as well as ultrafast response and recover time comparable to those exhibited in those publications.

Conclusion:

It is demonstrated in our experiments that TiO₂ induction layer in 2D MoS₂ system can be used to significantly enhance PD performances. A significant increase in photocurrent was observed when the PDs were illuminated with a 650 nm light at very weak power density, giving the photoresponsivity and detectivity of 130 A/W and

 6.24×10^{12} J, respectively, under light power density of 1.6×10^{-6} W/cm² and RT. Furthermore, the response and recovery time of the v-MoS₂/TiO₂ PD were both less than 0.1 s.

The photoresponse behaviors were kept stable even at a temperature as high as 200°C. It was found that the detector was giving a maximum photoresponsivity and detectivity of 50 A/W and 2.3×10^{12} J, respectively, at 200 °C, thus offering potential applications for high temperature and reliable visible light detection. The FET structure of the PDs under -5 V gate voltage further improve the high-temperature performances at 200 °C, with low noise and higher photocurrent and detectivity than the situations under 5 V or without gate voltage. The results prove the potential application of v-MoS₂/TiO₂ heterostructures FET devices as visible light PD.

Acknowledgement:

This work was supported in part by the National Natural Science Foundation of China under Grant 62176220, in part by the Fundamental Research Funds for the Central Universities under Grant SWU020011.

Reference:

- [1] M. Razeghi, A. Rogalski, Semiconductor ultraviolet detectors, J. Appl. Phys. 9 (10) (1996) 7433–7473.
- [2] N. Ansari, F. Ghorbani, Light absorption optimization in two-dimensional transition metal dichalcogenide van der Waals heterostructures, J. Opt. Soc. Am. B 35 (5) (2018) 1179–1185.
- [3] B. Radisavljevic, A. Radenovic, J. Brivio, I.V. Giacometti, A. Kis, Single-layer MoS₂ transistors, Nat. Nanotechnol. 6 (3) (2011) 147.
- [4] S. Li, S. Wang, M.M. Salamone, A.W. Robertson, S. Nayak, H. Kim, S.E. Tsang, M. Pasta, J.H. Warner, Edge-enriched 2D MoS₂ thin films grown by chemical vapor deposition for enhanced catalytic performance, ACS Catal. 7 (1) (2016) 877–886.
- [5] H. Li, H. Wu, S. Yuan, H. Qian, Synthesis and characterization of vertically standing MoS₂ nanosheets, Sci. Rep. 6 (2016) 21171.

- [6] N.Zhou, R. Wang, X. Zhou. H. Song, X. Xiong, Y. Ding, J. Lü, L. Gan, T. Zhai, P-GaSe/N-MoS₂ vertical heterostructures synthesized by van der waals epitaxy for photoresponse modulation, Small 14 (2018) 1702731.
- [7] R. Korde, J. Geist, Stable, high quantum efficiency, UV-enhanced silicon photodiodes by arsenic diffusion, Solid-State Electron. 30 (1) (1987) 89-92.
- [8] Y. Koide, M. Liao, J. Alvarez, Thermally stable solar-blind diamond UV photodetector, Diamond Relat. Mater. 15 (2006) 1962-1966.
- [9] P.F. Satterthwaite, A.S. Yalamarthy, N.A. Scandrette, A.K.M. Newaz, D.G. Senesky, High responsivity, low dark current ultraviolet PDs based on two-dimensional electron gas interdigitated transducers, ACS Photonics 5 (2018) 4277–4282.
- [10] M. Garg, B.R. Tak, R.V. Ramgopal, R. Singh, Enhanced performance of MSM UV PDs by molecular modification of gallium nitride using porphyrin organic molecules, IEEE Trans. Electron Devices 66 (2019) 2036–2039.
- [11] B.R. Tak, M. Garg, A. Kumar, V. Gupta, R. Singh, Gamma irradiation effect on performance of β-Ga₂O₃ metal-semiconductor-metal solar-blind PDs for space applications, ECS J. Solid State Sci. Technol. 8 (2019) 3149–3153.
- [12] H.-J. Song, M.-H. Seo, K.-W. Choi, M.-S. Jo, J.-Y. Yoo, J.-B. Yoon, High-performance copper oxide visible-light photodetector via grain-structure model, Sci. Rep. 9 (2019) 7334.
- [13] A. Zhang, S.F. You, C. Soci, Y.S. Liu, D.L. Wang, Y.H. Lo, Silicon nanowire detectors showing phototransistive gain, Appl. Phys. Lett. 93 (12) (2008) 121110
- [14] J.D. Hwang, Y.K. Fang, K.H. Wu, S.M. Chou, Improving breakdown voltage of SiC/Si heterojunction with graded structure by rapid thermal CVD technology, IEEE Trans. Electron Devices, 44 (1997) 2029–2031
- [15] K. Zhang, S.L. Feng, S. Kang, Y.T. Wu, Q. Wang, Z. Tao, Y. Fan, W.Q. Lu, Dynamically induced large-scale, selective, and vertical structure growth of MoS₂ nanosheets, Adv. Eng. Mater. (2021) 2101105.
- [16] M.A. Kang, J.K. Han, S.Y. Cho, S.D. Bu, C.Y. Park, S. Myung, W. Song, S.S. Lee, J. Lim, K.S. An, Strain-gradient effect in gas sensors based on three-dimensional hollow molybdenum disulfide nanoflakes, ACS Appl. Mater. Interfaces 9 (2017) 43799–43806
- [17] S. Liu, C. Nie, D. Zhou, J. Shen, S. Feng, Direct growth of vertical structure MoS₂ nanosheets array film via CVD method for photodetection, Phys. E (Amsterdam, Neth.) 117 (2020) 113592.

- [18] Y. Liu, M. Guo, Z. Liu, Q. Wei, M. Wei, Rapid and facile synthesis of hierarchically mesoporous TiO₂₋B with enhanced reversible capacity and rate capability, J. Mater. Chem. A 6 (3) (2018) 1196-1200.
- [19] X. Xue, W. Ji, Z. Mao, H. Mao, Y. Wang, X. Wang, W. Ruan, B. Zhao, J. Lombardi, R. John, Raman investigation of nanosized TiO₂: effect of crystallite size and quantum confinement, J. Phys. Chem. C 116 (15) (2012) 8792-8797.
- [20] S. Balaji, Y. Djaoued, J. Robichaud, Phonon confinement studies in nanocrystalline anatase-TiO₂ thin films by micro Raman spectroscopy, J. Raman spectrosc. 37 (12) (2006) 1416-1422.
- [21] L. Guo, Z. Yang, K. Marcus, Z. Li, B. Luo, L. Zhou, X. Wang, Y. Du, Y. Yang, MoS₂/TiO₂ heterostructures as nonmetal plasmonic photocatalysts for highly efficient hydrogen evolution, Energy Environ. Sci. 11 (1) (2017) 106-114.
- [22] L. Zheng, S. Han, H. Liu, P. Yu, X. Fang, Hierarchical MoS₂ nanosheet@TiO₂ nanotube array composites with enhanced photocatalytic and photocurrent performances, Small 12 (11) (2016) 1527-1536
- [23] H. Li, Y. Wang, G. Chen, Y. Sang, H. Jiang, J. He, X. Li, H. Liu, Few-layered MoS₂ nanosheets wrapped ultrafine TiO₂ nanobelts with enhanced photocatalytic property, Nanoscale 8 (11) (2016) 6101-6109.
- [24] X. Peng, Y. Han, Q. Zhang, P. Feng, P. Jia, H. Cui, L. Wang, and S. Duan, Performance Improvement of MoS₂ Gas Sensor at room temperature, IEEE Trans. Electron Devices. 68 (9) (2021) 4644-4650
- [25] K. Hannes, H. Yan, M. Benjamin, L. Matthew, P. Yang, Nanowire ultraviolet photodetectors and optical switches, Adv. Mater. 14 (2) (2002) 158-160.
- [26] B. Cho, K. Ra, Y. Park, Y. Jongwon, Y.J. Lee, S. Lee, T.J. Yoo, C.G. Kang, B.H. Lee, H. Ko, Bifunctional sensing characteristics of chemical vapor deposition synthesized atomic-layered MoS2, ACS Appl. Mater. Interfaces 7 (4) (2015) 2952-2959
- [27] J. Jie, W. Zhang, Y. Jiang, X. Meng, Y. Li, S. Lee, Photoconductive characteristics of single-crystal CdS nanoribbons, Nano Lett. 6 (9) (2006) 1887-1892.
- [28] C. Soci, A. Zhang, B. Xiang, S. Dayeh, D. P. Aplin, J. Park, X. Bao, Y.H. Lo, D. Wang, ZnO nanowire UV photodetectors with high internal gain, Nano Lett. 7 (4) (2007) 1003-1009.
- [29] X. Cao, P. Chen, Y. Guo, Decoration of textured ZnO nanowires array with CdTe quantum dots: enhanced light-trapping effect and photogenerated charge separation, J. Phys. Chem. C 112 (51) (2008) 20560–20566.

- [30] X. Wang, Y. Xiao, D. Zeng, C. Xie, Optimizing the packing density of TiO₂ nanorod arrays for enhanced light harvesting by a light trapping effect and its photocatalytic decomposition of gaseous benzene, Cryst. Eng. Comm. 17 (5) (2015) 1151–1158.
- [31] R. Zou, Z. Zhang, Q. Liu, J. Hu, L. Sang, M. Liao, and W. Zhang, High detectivity solar-blind high-temperature deep-ultraviolet photodetector based on multi-layered (100) Facet-Oriented β-Ga₂O₃ nanobelts, small, 10(9) (2014) 1848–1856.
- [32] B. Rahmati, I. Hajzadeh, M. Taheri, R. Karimzadeh, S. Mohajerzadeh, S.M. Mohseni, Plasmonic improvement photoresponse of vertical-MoS₂ nanostructure photodetector by Au nanoparticles, Appl. Surf. Sci. 490 (2019) 165-171.
- [33] S. Sahin, M. Monika, S. Kaushik, S. Rajendra, High-temperature performance of a GaSe nanosheet-based broadband photodetector, ACS Appl. Electron. Mater. 2 (2020) 670–676.
- [34] M. Monika, A. Singh, B.R. Tak, R. Singh, Study of the photoresponse behavior of a high barrier Pd/MoS₂/Pd photodetector, J. Phys. D: Appl. Phys. 52 (32) (2019) 325102.
- [35] E. Yalon, C.J. McClellan, K.H. Smithe, R.M. Muñoz, R.L.Xu, Suryavanshi, V.Saurabh, A.J. Gabourie, J. Alex, M. Christopher, X. Feng, A.B. Farimani, Energy dissipation in monolayer MoS₂ electronics, Nano Lett. 17 (6) (2017) 3429-3433.
- [36] Xie, Y., Zhang, B., Wang, S., et al. (2017). Ultrabroadband MoS₂ Photodetector with Spectral Response from 445 to 2717 nm. Adv. Mater., 29(17), 1605972.
- [37] Yu, S. H., Lee, Y., Jang, S. K., et al. (2014). Dye-Sensitized MoS₂ Photodetector with Enhanced Spectral Photoresponse. ACS Nano, 8(8), 8285-8291.
- [38] Kufer, D., & Konstantatos, G. (2015). Highly Sensitive, Encapsulated MoS₂ Photodetector with Gate Controllable Gain and Speed. Nano Lett., 15(11), 7307-7313.
- [39] Wang, X., Wang, P., Wang, J., et al. (2015). Ultrasensitive and Broadband MoS₂Photodetector Driven by Ferroelectrics. Adv. Mater., 27(42), 6575–6581.
- [40] Wang, W., Zeng, X., Warner, J. H., et al. (2020). Photoresponse-bias Modulation of High-Performance MoS₂ Photodetector with Unique Vertically Stacked 2H-MoS₂/1T@2H-MoS₂ Structure. ACS Appl. Mater. Interfaces 2020, 12, 33325–33335.
- [41] Chen, Z., ZHANG, Z., Biscaras, J., & Shukla, A. (2018). High performance self-driven photodetector based on graphene/ InSe/MoS₂ vertical heterostructure. J. Mater. Chem. C, 6(45), 12407-12412.
- [42] Zhang, R., Ma, X., An, C., Zhang, D., Sun, D., Hu, X., & Liu, J. (2019). Self-powered photodetector based on vertical MoO₃/MoS₂ heterostructure with gate tunable photoresponse. 2D Materials, 6(3) (2019) 035033.

- [43] Kumar, R., Goel, N., Raliya, R., Biswas, P., & Kumar, M. (2018). High-performance photodetector based on hybrid of MoS₂ and reduced graphene oxide. Nanotechnology, 29(40), 404001.
- [44] Chakrabarti, S., Stiff-Roberts, A. D., Bhattacharya, P., Gunapala, S., Bandara, S., Rafol, S. B., & Kennerly, S. W. (2004). High-Temperature Operation of InAs-GaAs Quantum-Dot Infrared Photodetectors with Large Responsivity and Detectivity. IEEE Photonic. Tech. Lett., 16(5), 1361-1363.
- [45] Sorifi, S., Moun, M., Kaushik, S., & Singh, R. (2020). High temperature performance of GaSe nanosheet based broadband photodetector. ACS Appl. Electro. Mater. 2020, 2(3), 670-676.